POLITECNICO DI TORINO
Repository ISTITUZIONALE

Rockburst characteristics of gypsum-like rocks after fatigue cyclic loading

Original
Rockburst characteristics of gypsum-like rocks after fatigue cyclic loading / Wang, C., Wei, S., Wang, M., Xu, C., Zhang, S.. - In: ARABIAN JOURNAL OF GEOSCIENCES. - ISSN 1866-7511. - 15:15(2022). [10.1007/s12517-022-10636-y]

Availability:
This version is available at: 11583/2997265 since: 2025-02-06T14:33:20Z

Publisher:
Springer Nature

Published
DOI:10.1007/s12517-022-10636-y

Terms of use:

This article is made available under terms and conditions as specified in the corresponding bibliographic description in the repository

Publisher copyright

(Article begins on next page)

17 November 2026

Rockburst characteristics of gypsum-like rocks after fatigue cyclic loading

Wang Chongyang[1], Wei Sijiang[1], Wang Meng[1], Xu Chongbang[2], Zhang Sheng[1]

1-School of Energy Science and Engineering, Henan Polytechnic University, Jiaozuo, Henan 454000.

2-Bridge and Tunnel Research Center, Institute of Highway Science, Ministry of Transport, Beijing 100089, China.

* Correspondence: jzitwsj@126.com

Abstract: In underground engineering applications, surrounding rock is often subjected to dynamic disturbances, such as vehicle loading, earthquakes, blasting, or other vibrations. Consequently, fatigue damage, collapse, and rock burst may happen. In this study, a dynamic fatigue rock mechanics testing machine was used to study the rock burst characteristics of gypsum rocks before and after cyclic loading. With increasing fatigue frequency, the energy consumed by each loading and unloading cycle and the accumulated fatigue damage gradually increase. Hysteresis loops of the stress-strain curve gradually transition from elongated to near circular, and the area of loops gradually increases. With increasing loading time, the damage variable of the sample increases, while the growth rate decreases, which conforms to a logarithmic growth law. At a central value of fatigue loading C = 9 MPa, the uniaxial compressive strength of specimens weakened, but increased in response to high frequency fatigue loading. For C = 18 MPa, the jitter adjustment trend in the post-peak strength phase became apparent, which led to a decrease of rock burst trend. At C = 27 MPa, the rock burst tendency increased significantly. The acoustic emission characteristics correspond well with both the loading process and full stress-time curves. Several indexes (i.e., impact energy, elastic energy, and elastic modulus) follow a quadratic nonlinear relationship with loading frequency, which can be used to predict rock burst tendency.

Key words: high strength gypsum; fatigue loading; rock burst; acoustic emission

1. Introduction

Rock burst is a common engineering disaster in deep buried high ground stress engineering. When it happens, the engineering progress will be seriously affected, which likely leads to casualties. For example, when the ore body enters deep mining, because of the pressure of overlying strata and the existence of high ground stress, the rock mass is in a state of high stress, causing it to be easily affected by dynamic loads such as blasting and mechanical vibration, thus causing accidents (Li et al. 2011). Moreover, under the action of mining stress, the rock is affected by cyclic stress, and rock burst characteristics may change, causing new instability. Therefore, it is of great significance to study the characteristics of rock burst in response to cyclic loading.

Recent studies showed that loading stress, loading frequency, test temperature, and other factors exert different degrees of influence on the fatigue characteristics of rock (Zuo et al. 2011; Li et al. 2010; Zhao 2013; Guo et al. 2011; Bai 2012; Li et al. 2016; Faradonbeh R S et al. 2020, 2021). With increasing loading stress (both upper limit stress and stress amplitude), the fatigue life of rock tends to decrease (Xiao 2009). However, there are two different viewpoints on the influence of loading frequency on fatigue characteristics. Several scholars suggested that a higher loading frequency will lead to a greater fatigue damage and a shorter fatigue life (Xiao 2009; Jiang 2003), while other scholars held the opposite view (Zhao 2013; Bagde and Petro 2005; Li et al. 2001; Ishizuka and Abe 1990). In terms of rock burst characteristics, both the elastic energy index (Kidybinski 1981) and the impact energy index (Goodman 1980) are commonly used indexes for measuring rock burst characteristics. The elastic energy index refers to the ratio of elastic energy and dissipated strain energy at a rock loading of 0.7-0.8 σ_c. The reverse bend point of volumetric strain can be used as unloading control point (Zhang et al. 2017). On this basis, a variety of indicators and methods for evaluating rock burst characteristics of rocks under different conditions have been developed (Pei et al. 2014; Cai et al. 2013; Yin et al.2014; Guo et al. 2015; Hu et al. 2019). For example, for main rocks at depth, three criteria (i.e., brittleness coefficient, linear elastic energy, and impact performance evaluation) are often used for the qualitative analysis of rock burst liability. For specific major deep rock engineering

applications in China, a rock burst classification prediction model has been established to predict rock burst (Guo et al. 2015).

Although considerable research has focused on rock fatigue and rock burst characteristics, rock burst characteristics after fatigue damage of rocks under different frequencies and loads has received little attention. Sampling natural rock remains difficult. In this experimental study, to control independent variables and reduce the influence of rock anisotropy on the experimental results, similar materials were used. Through many preliminary tests, gypsum rocks were found to have the characteristics of high strength and good homogeneity (Wei 2020). Therefore, the physical as well as mechanical properties and rock burst characteristics of gypsum rock samples after fatigue load have been studied to provide a reference for the control of surrounding rock in deep well mining engineering and underground engineering applications subject to impact dynamic load.

2. Materials and methods

2.1. *Sample preparation*

A grade α high strength gypsum powder, produced by Sichuan Hongtai Biochemical Co., Ltd., Nanchong, China, was selected. Its main component is $CaSO_4 \cdot 0.5H_2O$, and a block was poured according to a ratio of water to paste of 3:10, and a standard sample was processed. The specific preparation process is described in the following:

(1) Mold preparation: A cube mold with a side length of 20 cm was used and lubricating oil was applied on the inner surface to facilitate mold release, as shown in Figure 1(a).

(2) Production of the block: Gypsum powder was evenly poured into water, and the mixture was poured into the mold after full mixing for 90 s with a mixer. The mixture was placed on a vibrating table for 2 min to eliminate bubbles in the slurry and after heat loss, demodulation started. The finished test block is shown in Figure 1(b).

(3) Standard sample processing: After demolding, the test block was shaped into a cylindrical standard sample of 50 mm × 100 mm (Φ × h), which was then put into an oven at 45 ℃ for 48 h. At a quality difference between the two adjacent samples of less than 0.5 g, the sample described in this paper was obtained.

(4) Grouping: The samples were divided into three groups (I, II, and III) for fatigue loading test and rock burst characteristic test. All fatigue tests were conducted in the elastic stage. The central value of fatigue loading (C) of the three groups of samples was 0.2 σ_c, 0.4 σ_c, and 0.6σ_c for groups I, II, and III, respectively. Loading frequencies (f) of 1, 2, 4, 10, and 20 Hz were applied, the loading time (t) was 500 s, and the amplitude (A) was 0.1 σ_c, as shown in Table 1. To improve the reliability of the experimental results, six samples were prepared for each group, resulting in a total of 90 samples.

According to previous tests (Figure 2), the average uniaxial strength σ_c and average elasticity modulus E_T of gypsum rock-like samples used in this paper in the natural state was about 45MPa and 4.79GPa respectively (Wei 2020). As can be seen from figure 2, the stress-strain curve of the sample is approximately linear in section AB. Point A is the "crack closure stress" of the sample, and point B is the "crack damage stress" of the sample. When fatigue loading is carried out in the range of 0.1-0.7 σ_c, the fatigue stress of the three groups of samples remains before the yield stage of the whole curve.

2.2. Testing device

2.2.1. Wave velocity testing device

Longitudinal wave testing of specimens was carried out before and after fatigue loading by using a UTA2001A ultrasonic tester, as shown in Figure 3(a). The instrument is simple to operate and has high reliability. The frequency response range is 1-500 kHz, the acoustic velocity range is 9.999 km/s, sampling frequencies of 10, 5, 2, and 1 MHz were applied, and the probe frequency was 12.5-500 kHz.

2.2.2 Acoustic emission testing device

Fracture information (i.e., acoustic emission ringing number and energy) of specimens during fatigue loading and static compression was measured with a DS5-8B holographic acoustic emission signal analyzer, as shown in

Figure 3(b). The acoustic emission (AE) instrument adopts a USB3.0 interface with 2-8 channels, and can be used for multi-channel synchronous acquisition. Sampling trigger modes are signal threshold trigger and external trigger. The continuous data pass rate is 65.5 MB/s, and the data pass rate reaches up to 393 MB/s.

2.2.3. Mechanical testing device

(1) Uniaxial compression test and rock loading and unloading tests were carried out on a RMT-150C electro-hydraulic servo rock test system, as shown in Figure 4(a) and (b). Axial load was measured by a 1000 kN force sensor with a load accuracy of 1.0×10^{-3} kN. Axial compression deformation was measured by a 5.0 mm displacement sensor with a deformation accuracy of 1.0×10^{-3} mm. During the test, displacement was adopted, and the loading rate was 0.005 mm/s.

(2) A fatigue loading test was carried out on a QKX-YD-1000 electro-hydraulic servo rock dynamic fatigue test machine, which was produced by Qingdao Qiankunxing Intelligent Technology Co., Ltd., Qingdao, Shandong Province. As shown in Figure 4(c) and (d). The maximum axial load of the system is 800 kN, the maximum loading speed is 800 mm/min, the fatigue frequency range is 0.5-50 Hz, and the maximum displacement is 50 mm.

2.3 Test methods

(1) Measuring sample size, mass, and longitudinal wave velocity: A Vernier caliper was used to measure the diameter and length of the sample, and the mass was weighed by an electronic scale. A Uta-2000a intelligent ultrasonic monitor was used to measure the longitudinal wave velocity at a sampling frequency of 10 MHz. Vaseline coupling was adopted between the sample end face and the sensor.

(2) Fatigue loading test: The force control mode used a loading rate of 0.5 kN/s. First, the sample was loaded under the specified load, and then, the fatigue test of the sample was carried out. The load used a sine wave. Figure 5 shows the load phase and load control method.

(3) Rock burst characteristic test: The uniaxial compression test adopts displacement control mode at a loading rate of 0.005 mm/s. The loading and unloading test adopt force control mode and a loading speed of 0.5 kN/s. The stress-strain during uniaxial compression and loading and unloading was obtained by loading 0.7-0.8 σ_c to unload.

(4) AE characteristic: In the process of fatigue loading and uniaxial compression testing, two channels were adopted to test the energy variation characteristics of samples.

3.Test Results and Analysis

3.1 Ultrasonic test result

The mean value of the longitudinal wave velocity and the corresponding standard deviation of the sample before fatigue load (V_0) and after fatigue load (V_P) are shown in Table 2. After fatigue loading, the wave velocity of the sample increased slightly, with groups I and III showing the most obvious increases of 2.1% and 1.4%, respectively. Group II increased slightly, by about 0.21%. Fatigue loading was carried out within a range of 0.1-0.7 σ_c, and the stress of the three groups of samples remained within the elastic stage range of the entire curve. In the process of fatigue loading, the longitudinal wave velocity of the sample increases because the gap between particles decreases and the wave velocity increases. The fatigue load is equivalent to the ‘exercise’ of the sample, which contributes to a smaller adjustment of micro-pores inside the sample, causing a slight increase in wave velocity. However, the influence of frequency on p-wave velocity was not obvious when the upper limit and middle limit of C remain fixed. The influence of the central value of fatigue loading on p-wave velocity is greater than that of frequency.

3.2 Fatigue properties

To save space, this paper only shows the stress-strain curve of the sample under $C = 0.6\sigma_c$. Because of high frequency and repeated cycles of loading and unloading, the hysteresis loops at typical fatigue loading times (t) of 50, 150, 250, 350, and 450 s were selected to analyze the damage variables, as shown in Figure 6. As mentioned above, although the upper limit of fatigue of the three groups of samples remained within the elastic range, corresponding damage occurred because of the adjustment of particle micro-pores inside samples. With increasing frequency, the hysteresis loop gradually transitioned from elongated to circular, and a higher frequency caused more

apparent damage. At a low loading frequency, the load on the sample changed slowly, the stress-strain curve increased gently, and the hysteresis loop sloped toward the strain axis, as shown in Figure 6(a) and (b). With increasing loading frequency, the loading and unloading speeds increased from 0.4 σ_c/s (1 Hz) to 8 σ_c/s (20 Hz). Moreover, the opening between the hysteresis loop loading and unloading gradually increased, indicating increasing sample damage, as shown in Figure 6(e). In addition, with increasing loading frequency, the area enclosed by the hysteresis loop gradually increased, and with increasing permanent damage, an overall right shift trend of hysteresis loop became obvious. However, the growth rate of this right shift gradually decreased, indicating that the growth rate of accumulated damage presents a decreasing trend with extended loading time.

To quantitatively analyze the effects of loading time and frequency on strain, the peak strain of each sample was extracted at typical moments, and the strain at the beginning of fatigue loading (ε_0) was taken as benchmark. The strain at typical moments (ε) was identified and the damage variable D at typical moments was calculated as follows:

$$D = \frac{\varepsilon - \varepsilon_0}{\varepsilon_0} \qquad (1)$$

The calculated results are shown in Table 3, where f is the loading frequency and t is the fatigue loading time.

As shown in Table 3, with extended loading time, the damage variation of the sample followed an increasing trend. To further analyze the relationship between damage variable D and loading time t or frequency f, logarithmic fit was applied, and the results are shown in Figure 6.

Figure 7 shows that with increasing loading time, the damage variable presented an increasing trend, and the growth rate was high during the early 0-50 s of loading, after which, it slowed down. The cumulative damage of the sample increased, but the growth rate decreased, which is consistent with the right shift of the hysteresis loop and the increase of plastic strain. At the same time, with increasing frequency, the damage variable attenuated. At low frequencies (1-2 Hz), the rate of decline was relatively high. With increasing frequency, the curve tended to flatten. The confidence of each $D(t)$ fitting function exceeded 0.98. The confidence of each $D(f)$ fitting function exceeded 0.84. This indicates that the fitting curve can predict the damage variable of the sample.

Figure 8 shows the stress-circumferential strain curve of the sample at typical moments. Compared with the stress-axial strain hysteretic curve, the stress-circumferential strain hysteretic curve has more step sizes and is not smooth. This is because, compared with the axial deformation, the circumferential deformation of the sample is not directly related to the axial pressure, and the stress-circumferential deformation deviates quicker from the linear elastic state. Comparing the hysteretic curve of the typical sample at different frequencies shows that at a low loading frequency, the inclination angle of the hysteretic line is tilted to the ε axis, the load of the sample changed slowly and the strain of the sample changed strongly. For example, when f = 1 Hz and f = 2 Hz were used, the differences between the annular strain peak value and the valley value of the average single hysteretic ring were 2.23×10^{-5} and 2.09×10^{-5}, respectively. With increasing loading frequency, the dip angle of the hysteretic loop gradually inclined toward the σ axis, the loading rate of the sample increased, and the variation range of the sample gradually decreased. For example, when f = 10 Hz and f = 20 Hz were used, the differences between the peak value and valley value of the annular strain of the average single hysteretic loop were 1.77×10^{-5} and 8.66×10^{-7}, respectively. In addition, with extended loading time, the left offset of the hysteretic loop increases, indicating that the damage of the specimen also increases.

The above analysis shows that the axial deformation of the sample is positive, which promotes volume deformation, while the circular deformation of the sample is negative, which hinders volume deformation to a certain extent. To quantitatively analyze the volume change of the sample during fatigue loading, the volume strain ε_V of the sample at a typical moment is calculated according to the following formula:

$$\varepsilon_V = \varepsilon_1 + \varepsilon_2 + \varepsilon_3 = \varepsilon_1 + 2\varepsilon_2 \qquad (2)$$

where, ε_1 is axial strain, ε_2 and ε_3 is circumferential strain.

According to Formula (2), the strain values of samples at each typical moment of fatigue stage are calculated, and the results are shown in Table 4. The influence of fatigue loading time on sample bulk strain was analyzed. At

t = 50 s, the average volume strain of the sample at typical time should be 3.24×10^{-3}. Compared with t = 50 s, the average volume strain of t = 150, 250, 350, and 450 s increased by 1%, 2.1%, 2.2%, and 2.6%, respectively. These results show that the volumetric strain of the sample increases with extended loading time, and the sample is gradually 'compacted' during fatigue loading.

During the loading process, the micro-pore expansion, closure, and slippage in the sample will cause the AE phenomenon. In this test, the damage characteristics under fatigue loading and subsequent uniaxial compression were evaluated by using the ringing count and energy of AE parameters. The curve of group $C = 0.6\ \sigma_c$ is shown in Figure 9.

Figure 9 shows that the AE phenomenon of the gypsum rock sample corresponds well with its whole-process stress-strain curve. The characteristics are shown in the following:

(1) Initial loading stage, I: In the process of uniform loading (0-0.6 σ_c), the overall AE ringing count is small, basically remaining within 200 times, and the energy is low, indicating that the sample is slightly damaged at this stage. The AE phenomenon is caused by the closure and compaction of micro-pores in the sample.

(2) Crack growth stage, II: When the axial stress of the sample reaches 0.6 σ_c, the specimen enters the fatigue loading stage. At this time, AE activities are significantly enhanced, ringing count and energy suddenly increase, and cracks and micro-pores in the sample begin to be adjusted on a large scale, which damages the sample.

(3) Fatigue loading stage, III: Under a fatigue load of 0.5-0.7 σ_c, the internal particles of the sample are constantly adjusted, the AE response is weakened and tends to stabilize, and the ringing count and energy change uniformly, especially when f = 4 Hz and f = 20 Hz are used. This is because after entering the fatigue loading stage, the stress of the specimen is cyclic stress with a constant vibration amplitude, and the state of the sample gradually tends to stabilize.

3.3 Rock burst feature

To compare the impact of fatigue loading on the rock burst characteristics of gypsum rock samples, the impact energy index K_E and elastic energy index W_{ET} of samples are compared before and after fatigue loading. The determination method is depicted in Figure 10. To calculate K_E, W_{21} (i.e., the energy accumulated by loading) is divided by W_{22} (i.e., the energy released by the destruction process). The calculation formula are shown in the following:

$$K_E = \frac{W_{21}}{W_{22}} \tag{3}$$

$$W_{21} = \int_0^{\varepsilon_3} \sigma \, d\varepsilon \tag{4}$$

$$W_{22} = \int_{\varepsilon_3}^{\varepsilon_4} \sigma \, d\varepsilon \tag{5}$$

To calculate W_{ET}, the sample needs to be loaded to 70-80% of the peak load for unloading. The plastic strain energy is W_{11}, the elastic strain energy is W_{12}, and the ratio between W_{12} and W_{11} is the elastic energy index W_{ET}. The calculation formula is as follows:

$$W_{ET} = \frac{W_{12}}{W_{11}} \tag{6}$$

$$W_{11} = \int_0^{\varepsilon_2} \sigma_j \, d\varepsilon - \int_{\varepsilon_1}^{\varepsilon_2} \sigma_x \, d\varepsilon \tag{7}$$

$$W_{12} = \int_{\varepsilon_1}^{\varepsilon_2} \sigma_x \, d\varepsilon \tag{8}$$

Statistical results of impact energy index and elastic energy index before and after fatigue are calculated according to Formulas (3) and (6), and the results are listed in Table 5. σ is the uniaxial strength, ε is the peak strain, and E_T is the elastic modulus (taking the slope of the peak strength of 30-70% approximate to the linear section).

3.3.1 Rock burst characteristics before fatigue

Figure 11 shows the stress-strain and load-unload curves of the whole process of uniaxial compression of gypsum rock samples before fatigue. Figure 11(a) shows that the stress-strain curve of uniaxial compression of each sample approximately follows the same changing rule, and all samples have undergone the four stages of compaction, elasticity, yield, and failure. (1) In the compaction stage, the stress-strain curve is concave. (2) In the elastic stage, the stress-strain curve is basically linear and follows Hooke's law. (3) In the yield stage, the increasing rate of axial stress gradually decreases, and the curve becomes concave. (4) In the failure stage, macroscopic slippage occurs along a certain fracture surface inside the sample, and both the deformation and damage of the sample are further aggravated. Table 4 shows that the average peak strength of the samples without fatigue loading is 45.7 MPa, the average impact energy index is 1.72, and the average elastic energy index is 2.78.

3.3.2 Impact characteristics after fatigue loading

Figure 12 shows the stress-strain curve of a typical sample during the whole process after fatigue loading. Figure 12(a) shows that in set I of samples with 0.1-0.3 σ_c axial stress fatigue load after 500 s, the trend of the stress strain curve is not apparent. All samples fall sharply after peak to the flow stage, showing clear rock burst tendency. The peak stress decreases at low frequencies, when f = 1 and 2 Hz, the uniaxial compression strengths of samples were 42.15 MPa and 34.4 MPa, which represent decreases by 7.77% and 24.7%, respectively, compared with samples without fatigue loading. At medium and high frequencies, the peak intensity increases. At f = 4, 10, and 20 Hz, uniaxial compression strengths were 46.01 MPa, 50.76 MPa, and 52.09 MPa, respectively. Compared with untired samples, the strength increased slightly, namely by 0.7%, 11.1%, and 14.0%, respectively. Regarding the impact energy index K_E, the average values of samples after fatigue at each frequency were 0.94, 1.34, 8.26, 9.17, and 2.48. Compared with before fatigue, at f = 1 and 2 Hz, K_E decreased by 45.3% and 22.1%, respectively. However, at other frequencies, the impact energy index increased: at f = 4, 10, and 20 Hz, K_E increase by 380%, 433%, and 44.2%, respectively. This is consistent with the variation trend of uniaxial peak intensity. The above conclusion indicates that under the condition of C = 0.2 σ_c, at low frequency (f = 1 or 2 Hz), Fatigue loading weakens the properties of samples, i.e., the uniaxial compressive strength and impact energy index of samples weakened to different degrees. When the frequency is high (f = 4, 10, and 20 Hz), the effect of fatigue loading on the sample is reinforced, which manifests as an exponential increase of the uniaxial strength and impact energy of the sample after cyclic loading.

Figure 12(b) shows that in set II of samples in the 0.3-0.5 σ_c axial stress fatigue load after 500 s, the stress-strain curve changes noticeably, which manifests as a weakening of brittleness, a strengthening of plasticity, and an increase of the post-peak curve jitter. The uniaxial compression strengths were 47.42 MPa (1 Hz), 41.48 MPa (2 Hz), 48.39 MPa (4 Hz), 47.23 MPa (10 Hz), and 44.21 MPa (20 Hz), which did not change significantly compared with the peak strength before fatigue. The impact energy indexes were 0.87, 0.88, 1.03, 2.59, and 1.49, the sample average was about 69.1% lower than that of set I, and compared to before fatigue, there was a downward trend, especially for f = 1 and 2 Hz, where the decrease was about 49%. The above analysis shows that when C = 0.4 σ_c the sample is greatly influenced. Although the uniaxial peak strength did not change significantly, the post-peak shake of the stress-strain curve was apparent. The impact energy index decreased greatly, which led to a decreasing rock burst tendency.

Figure 12(c) shows that the stress-strain curve of the sample changed more obviously after 500 s of axial stress fatigue loading at 0.5-0.7 σ_c. Except for the sample f = 2 Hz, the uniaxial peak strengths of all other samples increased, and at f = 4, 10, and 20 HZ, the impact energy indexes of samples were 79.9, 80.7, and 74.7, respectively, showing an explosive growth far beyond that of other samples. This indicates that at low frequency (f = 1 or 2 Hz), C = 0.6 σ_c has no apparent effect on samples. At high frequency (f = 4, 10, or 20 Hz), fatigue loading of 500 s causes a great change in sample properties, which manifests as a significant increase in the impact energy index and a surge in rock burst tendency.

Figure 13 shows the relationship between bell count, energy, stress, and time of the AE of samples under the condition of C = 0.6 σc. As shown in Figure 13, the AE phenomenon of samples is strongly correlated with the stage

of the whole process uniaxial compression curve. The characteristics are as follows:

(1) Initial loading stage, I: At this stage, the energy level is low, remaining mostly below 5000 mV*mS, and the AE ringing count is low, indicating that the rock damage at this stage is slight. After fatigue loading, most particle positions inside the sample have been adjusted, there are fewer dislocations between the particles, and there is only little deformation during reloading. This phenomenon is more apparent on the energy-time curve, especially Figure 13(b), (d), and (f).

(2) Crack stability expansion stage, II: Because of the continuous increase of external forces, new micro-cracks begin to appear in the rock mass, which gradually expand, and AE activities also increase to different degrees.

(3) Unsteady propagation of the crack to the failure stage, III: AE activities are significantly enhanced, and the ringing count and energy suddenly increase, reaching the maximum value. At this stage, cracks begin to connect with each other, which is characterized by clear stress concentration. Macroscopic cracks begin to form and expand, and eventually, the sample breaks.

(4) Post-peak stage, IV: The energy and ringing count of most samples decreases significantly because of sample rupture. For samples under low frequency (f = 1 and 2 Hz), loading still shows a certain post-peak residual stage, while for samples under high frequency (f = 4, 10, and 20 Hz), loading show obvious brittleness. The AE bell count, energy, and stress are identical, which suddenly drop to the low point after the peak, showing very poor impact resistance.

The relationship between the impact energy index K_E and frequency f of each group after fatigue is shown in Figure 14. K_E first increases and then decreases with increasing f. At f = 10 Hz, K_E reaches its maximum value, indicating that under this loading frequency, both the pores and cracks inside the sample reach the maximum degree of compaction, the brittleness of the sample increases, the stress slide accelerates after crushing, the amplitude of deformation decreases, the post-peak jitter decreases, and the impact energy index increases.

To quantitatively analyze the variation rule of the impact energy index with frequency, a quadratic polynomial ($K_E = a + bf + cf^2$) was used to fit three groups of data. The confidence of each curve exceeded 0.76, indicating that K_E and f presented a good nonlinear relationship. The confidence of the fitted quadratic curve was high.

3.3.3 Elastic energy index analysis

Figure 15 shows the loading and unloading curve after fatigue. In I and III sample sets, the elastic energy index in the low frequency variation is small ,but showing a significant reduction after f = 10 Hz. In II sample set, the low frequency results in slight increase of the elastic energy index, but with increasing frequency, the elastic energy index declined. Especially, for f = 20 Hz, the peak strain was nearly 5‰, and the elastic energy index fell to 1.2. This can be explained as follows: with increasing fatigue frequency, the elastic energy accumulated in the rock sample decreases gradually, the deformation of the sample increases gradually after loading to 0.7 σ_c, and the transient elastic strain decreases continuously after unloading. Because of these reasons, the ratio of elastic energy to plastic energy consumption of the sample decreases with increasing loading frequency, which is reflected in the loading and unloading curve, i.e., the right inclination of the curve and the elastic energy index decrease.

Figure 16 shows the relationship between elastic energy index W_{ET} and loading frequency f of each sample after fatigue. The coordinate corresponding to the dashed line (W_{ET} = 2.78) shows the average elastic energy index of the sample before fatigue loading. To quantitatively analyze the variation law of the elastic energy index with frequency, a quadratic polynomial ($W_{ET} = a + bf + cf^2$) was used to fit the two groups of data. As shown in Figure 16, the impact energy index and frequency are quadratically correlated. The fitting quadratic function opening is downward, and the curve is basically on the right side of the symmetry axis $K_E = -b / 2c$, which indicates that with increasing frequency, the declining rate of the impact energy index increases. The confidence of each curve exceeds 0.92, and this function can be used to predict the elastic energy index.

Figure 17 shows the relationship between the elastic modulus E_T and frequency f of each sample after fatigue loading. The coordinate corresponding to the dashed line in Figure 17 (E_T = 11.2 GPa) represents the average elastic

modulus of the sample before fatigue.

To quantitatively analyze the variation rule of elastic modulus with frequency, a quadratic polynomial (ET = a + bf + cf^2) was used to fit the two groups of data. The upward opening of the fitting curve indicates that E_T first decreases and then increases with increasing f. The confidence level of each curve exceeded 0.89, and the fitting result was good. The average elastic modulus of II group of samples was 13.95 GPa, while the average elastic moduli of groups I and III were 16.0% and 10.9%, respectively. This indicates that the reinforcement effect of group I and group III was most obvious under vibration fatigue loading. Appropriate stress loading not only effectively closes the original pores in the sample, but also prevents the sample from generating new cracks when subjected to excessive stress. This makes the sample more compact under vibration fatigue loading, which is reflected in the elastic modulus index, i.e., the deformation of the sample under the action of stress.

4. Discussion

As shown in Figure 6, with increasing fatigue frequency, the area surrounded by the hysteresis loop gradually increases, indicating that the amount of damage of the sample increases. To quantitatively analyze this change, the approximate area of each hysteretic loop is calculated by calculus.

As shown in Figure 18, the upper curve of the hysteresis loop is denoted by $A(\varepsilon)$ and the lower curve is denoted by $B(\varepsilon)$. Then, the calculation formula for the hysteresis loop area is:

$$S = \int_a^b A(\varepsilon)\, d\varepsilon - \int_a^b B(\varepsilon)\, d\varepsilon \qquad (9)$$

It can be approximated that:

$$S = \sum_{n=a}^{b} \triangle \varepsilon \left(\frac{A(n+\triangle\varepsilon)+A(n)}{2} - \frac{B(n+\triangle\varepsilon)+B(n)}{2} \right) \quad (10)$$

According to Formula (10), the hysteresis loop area of each sample during the first cycle is calculated, and the results are shown in Figure 19.

Figure 19 shows that the hysteresis loop area S is positively correlated with both C and frequency f in vibration. At C = 0.6 σ_c, the average hysteresis loop area was 1.74, which was 37.8% and 45.8% larger compared with C = 0.4 and 0.2 σ_c, respectively. At constant C, the growth rate of S reaches the maximum in the interval of $f \in$ [1,4] and decreases gradually when f exceeds 4 Hz.

The above analysis shows that the hysteresis loop area is closely related to the vibration-neutralization loading frequency: At low stress, the sample suffers less damage, and the transient elastic strain is large during unloading, resulting in a small hysteresis loop area. With increasing stress, the plastic strain energy gradually increases, while the transient elastic strain remains small during unloading, and the hysteresis loop area increases. At a low frequency, the sample is subjected to a small change rate of axial stress per unit time, the stress-strain curve mostly circulates along the direction of the stress-loading curve, and the hysteresis loop has a small opening and a small area. At high frequency, the change amplitude of axial stress in unit time increases synchronously, the rise and fall of stress-strain curve become more apparent, the dip angle and opening of the hysteresis loop increase, and the internal area gradually increases.

This result is consistent with the calculation results of damage variables shown in Section 3.2. The damage variable can be used to calculate the strain increase rate in the cumulative period, i.e., the total right deviation of the hysteresis loop. The hysteresis loop area can be used to calculate the energy consumption of a single hysteresis loop. At high frequencies, a single hysteresis loop has a large area and consumes more energy, but the hysteresis loop shows less right deviation; therefore, the damage per unit time is less. At low frequencies, although the area of a single hysteretic ring is small, the space between each hysteretic ring is large, and the overall energy consumption increases.

5. Conclusion

In this paper, remolded samples were cast with A-grade α-high strength gypsum powder. Remolded samples were tested by ultrasonic, fatigue loading, uniaxial compression, and acoustic emission tests. Fatigue and rock burst characteristics of gypsum samples before and after fatigue load were studied. The following conclusions can be drawn:

(1) With increasing fatigue frequency, the energy consumed by loading and unloading cycles and the accumulated fatigue damage gradually increase. The hysteresis loop transitions from a strip to a near circle, and its area increases.

(2) With extended loading time, the damage variable of the sample increases gradually, and the increase rate decreases gradually, which is in accordance with the growth law of the logarithmic function. With increasing frequency, the damage variable tends to decrease, and the rate of this decrease is higher at a frequency of 1-2 Hz, while the rate of decrease gradually decreases with increasing frequency.

(3) For samples under $C = 0.2\ \sigma_c$, the low-frequency fatigue load degrades and reduces the uniaxial compression strength of the sample, while the high-frequency fatigue load strengthens it. For the samples subjected to $C = 0.4\ \sigma_c$, the jittering adjustment trend after the peak of the curve of the whole process of uniaxial compression was apparent, leading to a decreasing rock burst tendency. After $C = 0.6\ \sigma_c$, the rock burst tendency increased significantly. The AE characteristics have good correspondence with the different stages of stress-time curve.

(4) The impact energy index, elastic energy index, elastic modulus, and loading frequency of samples before and after fatigue loading conform to the quadratic nonlinear relationship and can be used to predict the rock burst tendency of samples before and after fatigue loading.

Author Contributions: Wei Sijiang supervised the research and proposed the research direction. Wang Chongyang was responsible for the laboratory test, report analysis and paper writing. Wang Meng and Xu Chongbang helped in writing and re-checking the paper. Zhang Sheng helped with some laboratory test.

Funding: This work was supported by National Natural Science Foundation of China (No. 51974104)

Conflicts of Interest: The authors declare no conflict of interest.

References：

Bagde M N, Petros V (2005). Waveform effect on fatigue properties of intact sandstone in uniaxial cyclical loading[J]. Rock Mechanics and Rock Engineering, 38(3)：169–196.

Bai Yueming (2012). Experimental research on the fatigue property of salt rock under cyclic loading [M. S. Thesis] [D]. Chongqing：Chongqing University.

Cai Meifeng, Ji Dong, Guo Qifeng (2013). Study of rock burst prediction based on in-situ stress measurement and theory of energy accumulation caused by mining disturbance[J]. Chinese Journal of Rock Mechanics and Engineering,32(10): 1973–1980.

Faradonbeh R S, Taheri A, Karakus M (2020). Post-peak behaviour of rocks under cyclic loading using a double-criteria damage-controlled test method[J]. Bulletin of Engineering Geology and the Environment, 80(3).

Faradonbeh R S, Taheri A, Karakus M (2021). Failure Behaviour of a Sandstone Subjected to the Systematic Cyclic Loading: Insights from the Double-Criteria Damage-Controlled Test Method[J]. Rock Mechanics and Rock Engineering, 54(11):

Goodman R E (1980). Introduction to rock mechanics[M]. New York: John Wiley and Sons.

Guo Jianqiang, Zhao Qing, Wang Junbao, et al (2015). Rock burst prediction based on elastic stain energy[J]. Chinese Journal of Rock Mechanics and Engineering. 34(9): 1886–1892.

Guo Yintong, Zhao Kelie, Sun Guanhua, et al (2011). Experimental study of fatigue deformation and damage characteristics of salt rock under cyclic loading[J]. Rock and Soil Mechanics, 32(5)：1 353–1 359.

Hu Jie, He Manchao, Li Zhaohua, et al (2019). Experimental study of strain rockburst of anisotropic bedded sandstone [J]. Journal of China university of mining and technology, 48(04):735-741.

Ishizuka Y, Abe T (1990). Fatigue behaviour of granite under cyclic loading[C]// Static and Dynamic Considerations in Rock Engineering. Rotterdam：A. A. Balkema. 139–147.

Jiang Yu (2003). Fatigue failure and deformation development law of rock under cyclic load [M. S. Thesis] [D]. Shanghai：Shanghai Jiaotong University.

Kidybinski A (1981). Bursting liability indices of coal[J]. International Journal of Rock Mechanics and Mining Sciences, 18(6):295–304

Li Haoran, Yang Chunhe, Li Bailin, et al (2016). Damage evolution and characteristics of ultrasonic velocity and AE for salt rock under triaxial multilevel loading test[J]. Chinese Journal of Rock Mechanics and Engineering, 35(4)：683–691.

Li N, Chen W, Zhang P, et al (2001). The mechanical properties and a fatigue-damage model for jointed rock masses subjected to dynamic cyclical loading[J]. International Journal of Rock Mechanics and Mining Sciences, 38(7): 1 071–1 079.

Li Xiaojun, Lu Guangqi, Li Huamin (2010). Identification of the predictive information of rockmass failure based on the law of b-value change of AE events and its deficiency[J]. Journal of Henan Polytechnic University：Natural Science, 29(5)：663–666.

Li Xibing, Yao Jinrui, Gong Fengqiang (2011). Dynamic problems in deep exploration of hard rock metal mines[J]. The Chinese Journal of Nonferrous Metals, 21 (10): 2551 - 2563.

Pei Dianfei, Miao Shengjun, Long Chao, et al (2014). Rock burst tendency research based on a variety of criteria and gathered energy[J]. China Mining Magazine, 23(2): 79–83.

Wei Sijiang, Wang Chongyang, Yang Yushun, et al (2020). Physical and Mechanical Properties of Gypsum-Like Rock Materials[J]. Advances in Civil Engineering, doi:10.1155/2020/3703706.

Xiao Jianqing (2009). Theoretical and experimental study of rock fatigue characteristics under cyclic loading [Ph. D. Thesis] [D]. Changsha：Central South University.

Yin Zhiqiang, Li Xibing, Dong Longjun, et al (2014). Rock burst characteristics and proneness index under coupled static and dynamic loads[J].Journal of Central South University (Science and Technology), 45(9):3250–3256.

Zhang Chuanqing, Lu Jingjing, Chen Jun, et al (2017). Discussion on rock burst proneness indexes and their relation [J]. Rock and Soil Mechanics, 38(5):1397–1404.

Zhao Kai (2013). Experimental study on fatigue characteristics of karst areas limestone and engineering application [Ph. D. Thesis] [D]. Beijing：Beijing Jiaotong University.

Zuo Jianping, Pei Jianliang, Liu Jianfeng, et al (2011). Investigation on AE behavior and its time-space evolution mechanism in failure process of coal-rock combined body[J]. Chinese Journal of Rock Mechanics and Engineering, 30(8): 1 564–1 570.



(a) (b) (c)

FIGURE 1: gypsum sample. (a)Casting mould. (b)Cube sample. (c) standard sample

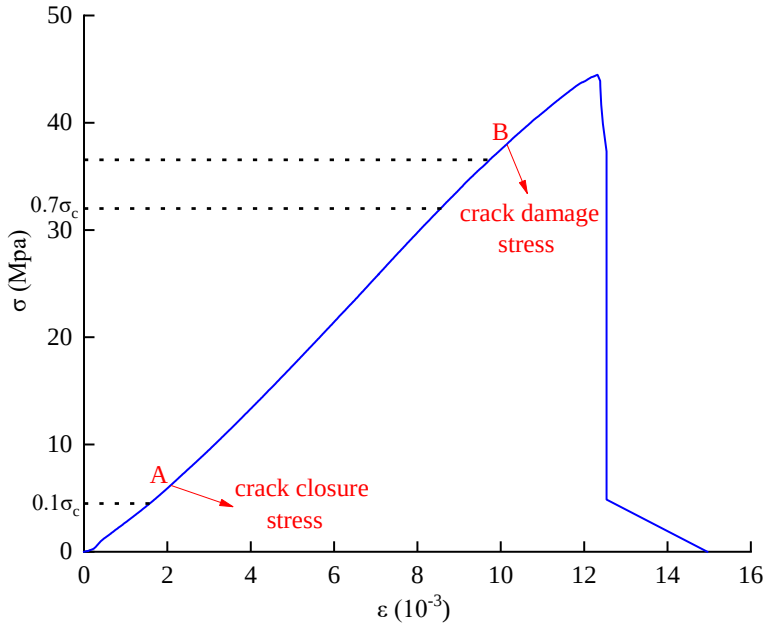
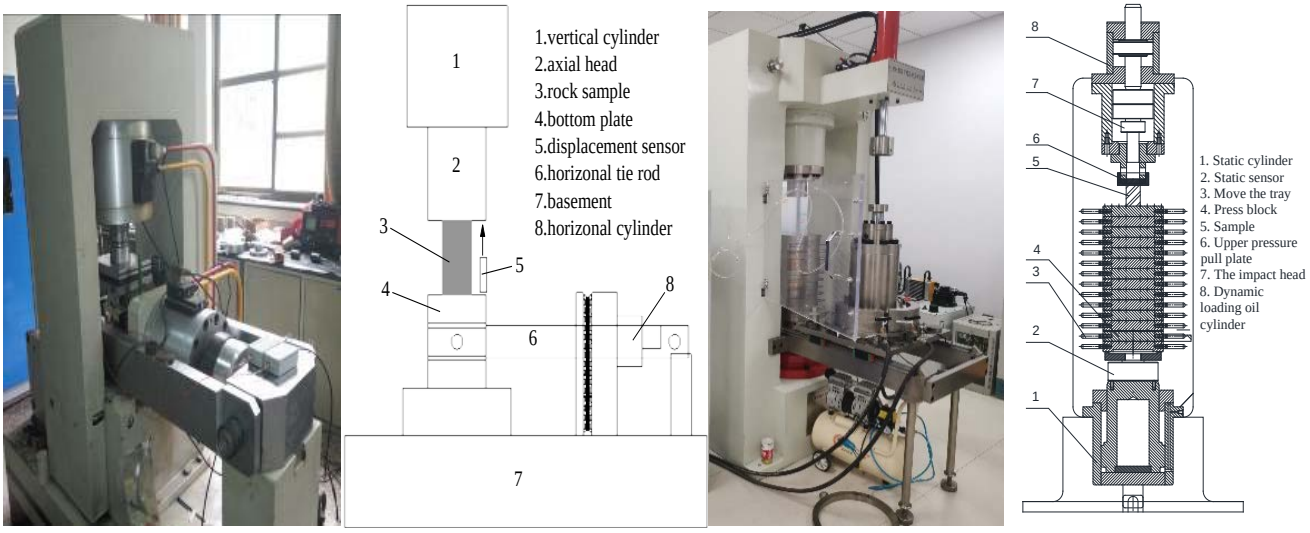


FIGURE 2: Full stress-strain curve of gypsum rock in natural state



(a) (b)

FIGURE 3: Acoustic testing apparatus. (a)Ultrasonic tester. (b)AE signal analyzer



(a) (b) (c) (d)

FIGURE 4: Mechanical testing device. (a) RMT-150B test system. (b) RMT-150B schematic diagram. (c) QKX-YD-1000 test system (d) QKX-YD-1000 schematic diagram..

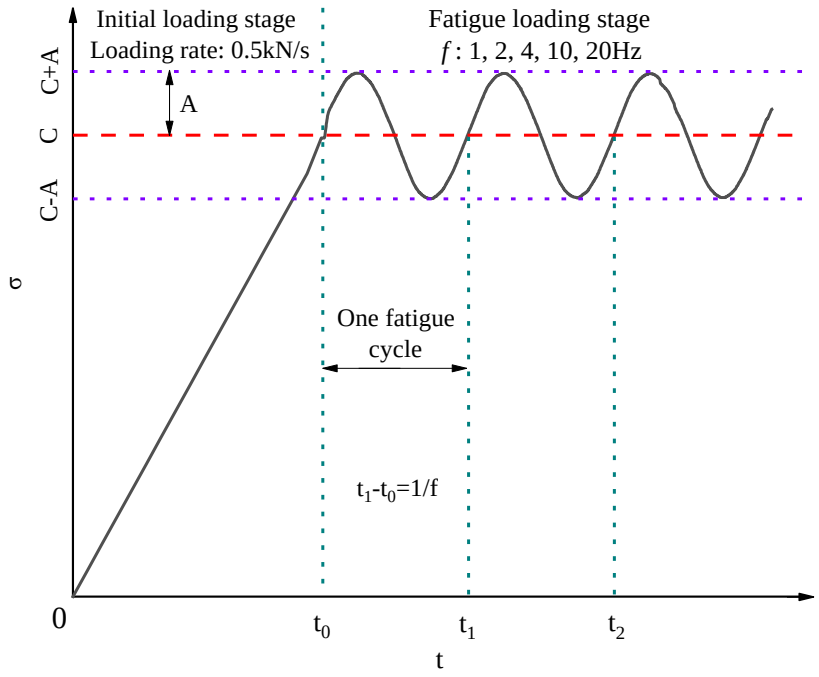


FIGURE 5: The different stages of loading with their load-control methods.

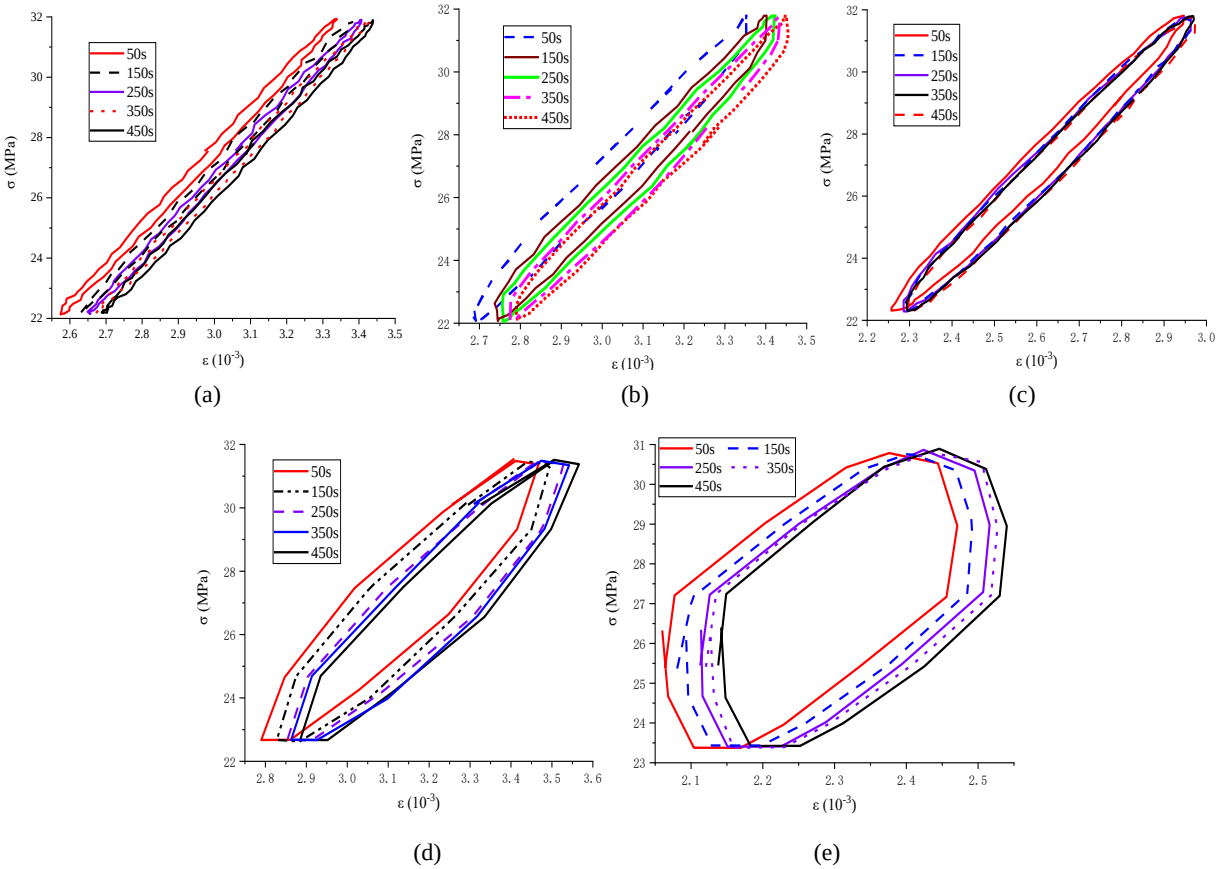
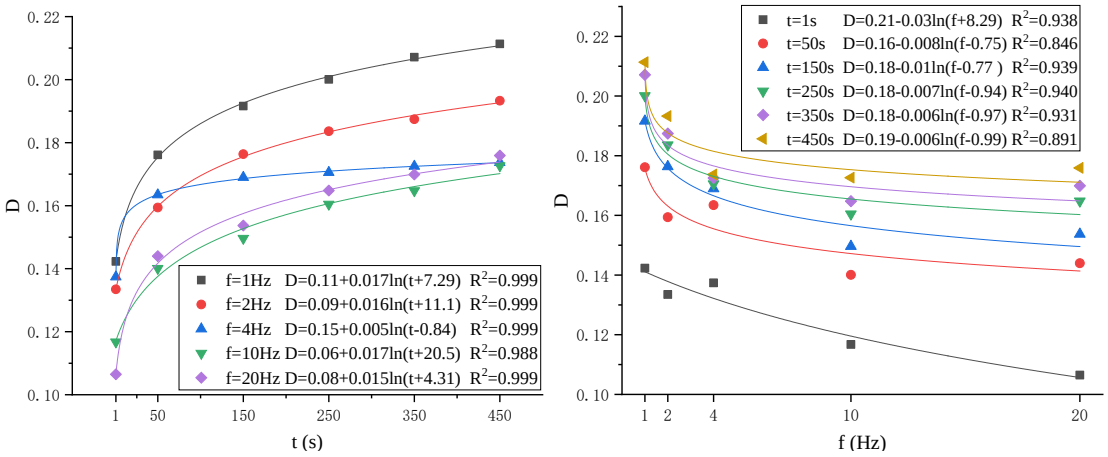
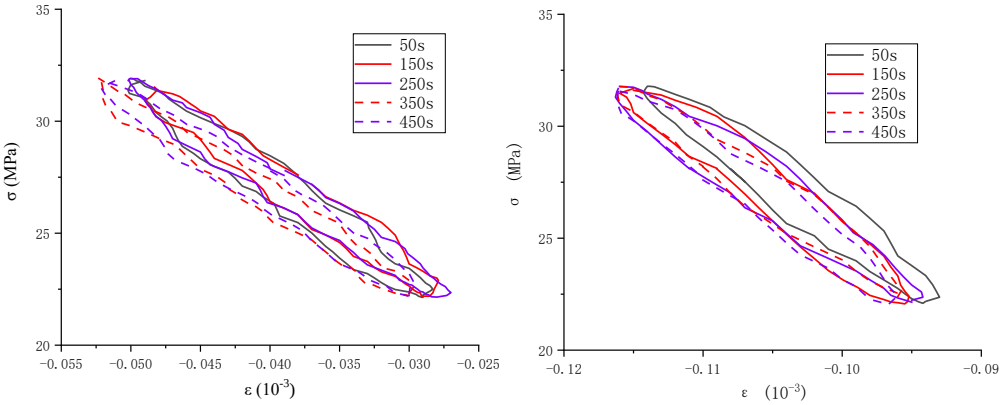


FIGURE 6: Hysteresis loop analysis at typical time. (a)*f*=1Hz. (b)*f*=2Hz. (c)*f*=4Hz. (d)*f*=10Hz. (e)*f*=20Hz.

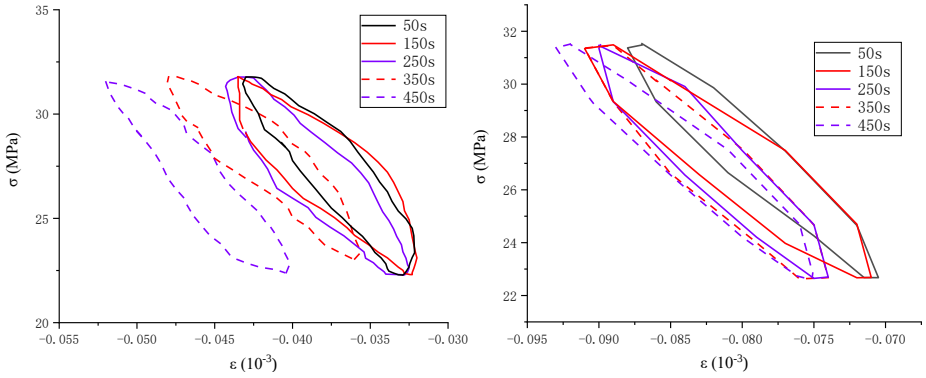


(a) (b)

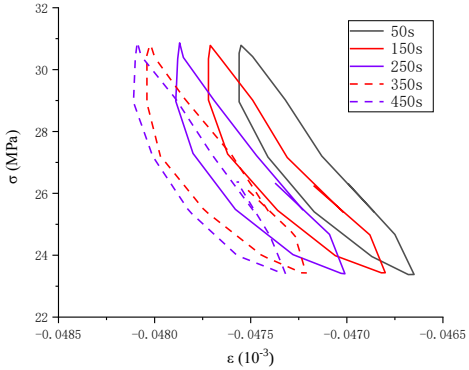
FIGURE 7: Damage variable fitting curve. (a)*D-t*. (b) *D-f*.



（a）f=1Hz （b）f=2Hz



（c）f=4Hz （d）f=10Hz



（e）f=20Hz

FIGURE 8: Stress-circumferential deformation curves at typical moments

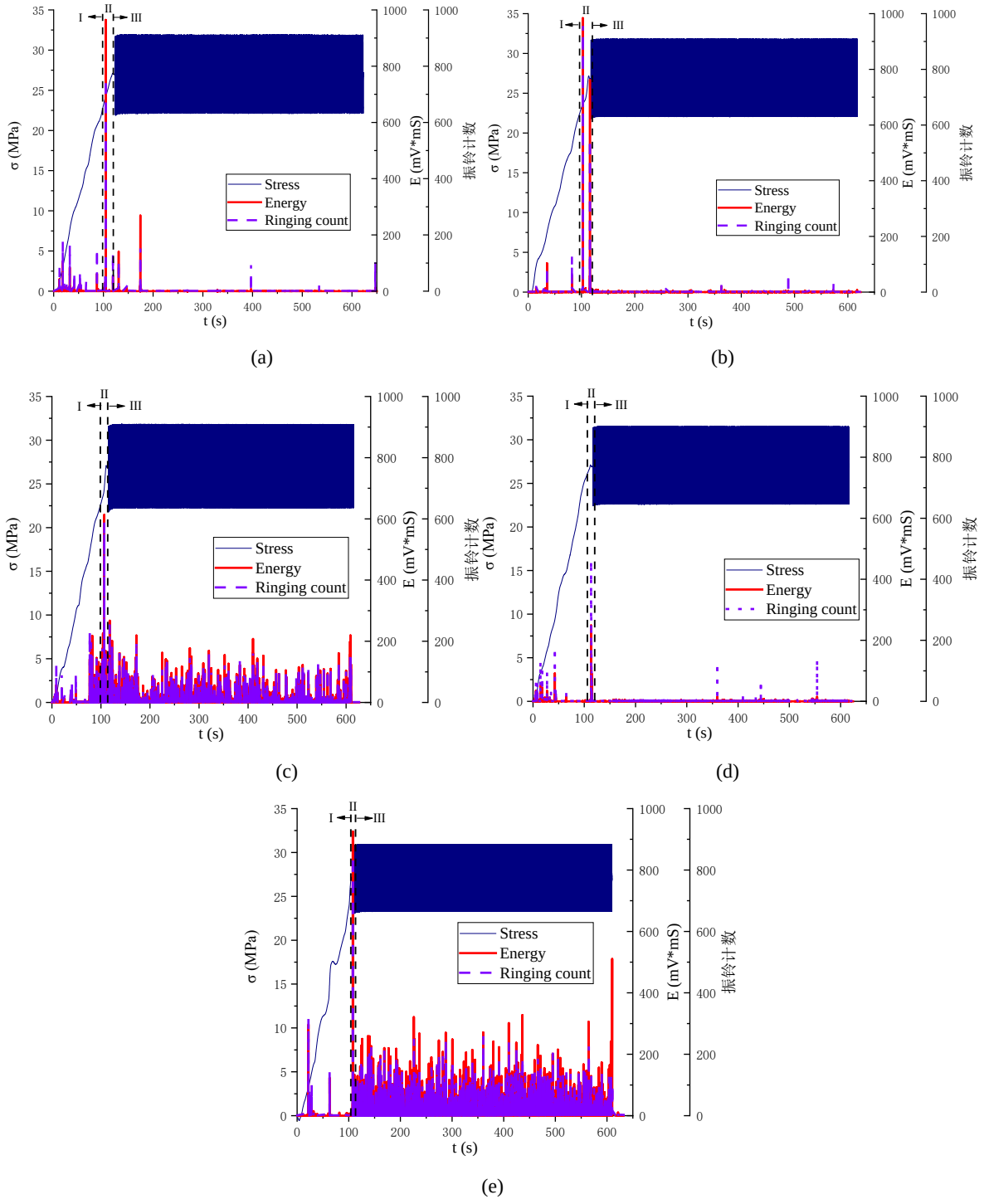


FIGURE 9: AE characteristics of gypsum rocks. (a)*f*=1Hz. (b)*f*=2Hz. (c)*f*=4Hz. (d)*f*=10Hz. (e)*f*=20Hz.

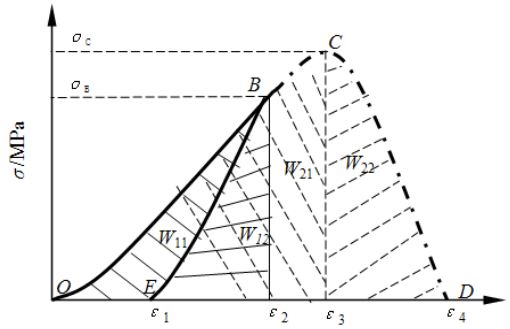
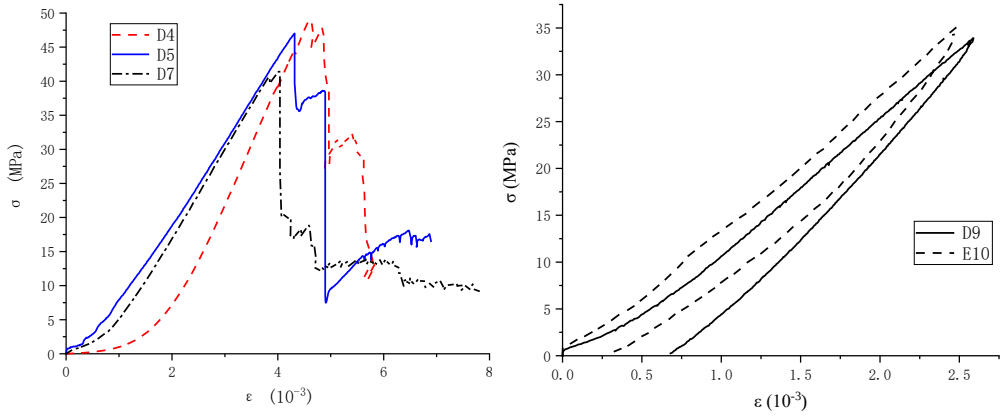
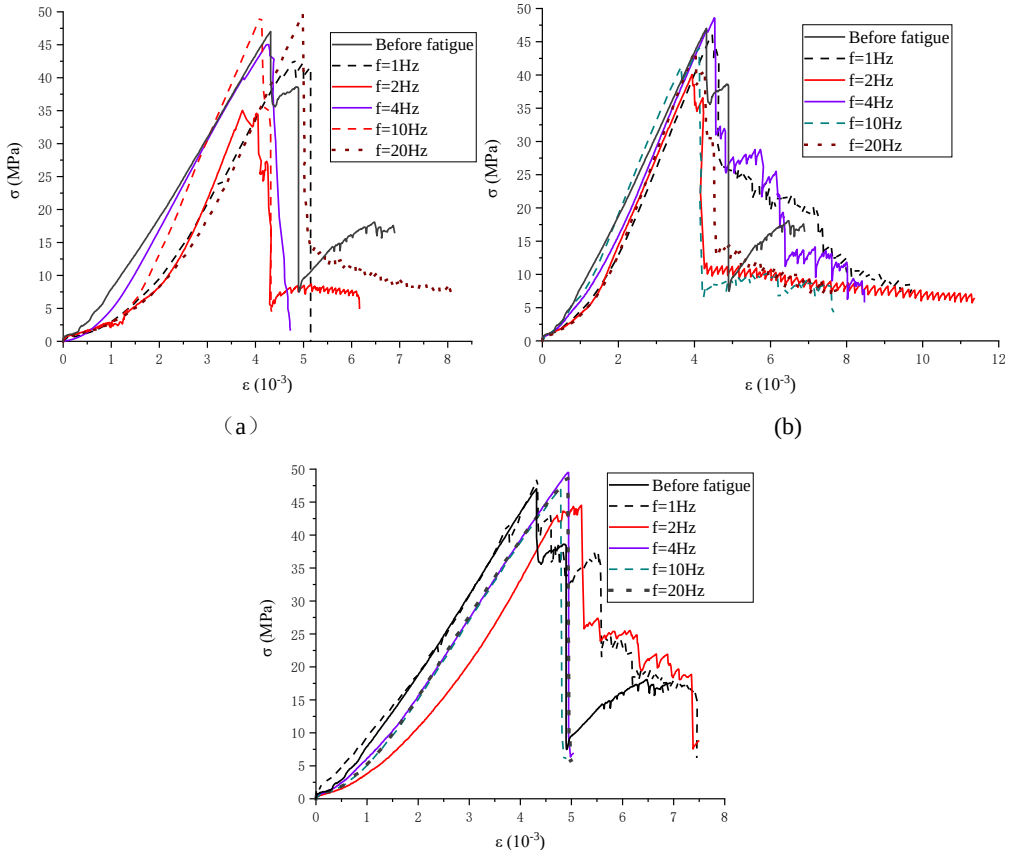


FIGURE 10: Calculation method of impact energy index and elastic energy index



(a) (b)

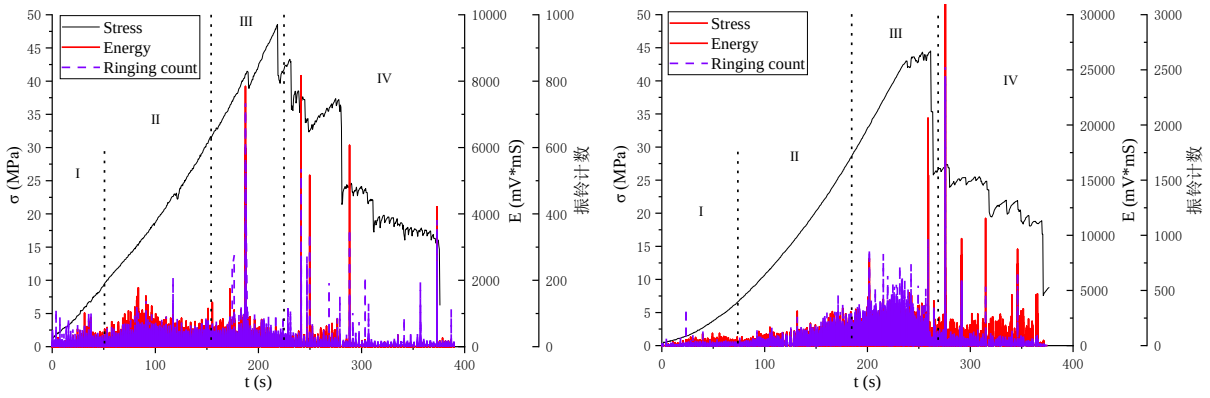
FIGURE 11: Test curve of the sample before fatigue.(a) Uniaxial compression. (b) Loading and unloading.



（a） (b)

(c)

FIGURE 12: Uniaxial compression test curve of samples. (a)C=0.2σ_c. (b)C=0.4σ_c. (c)C=0.6σ_c.



(a) (b)

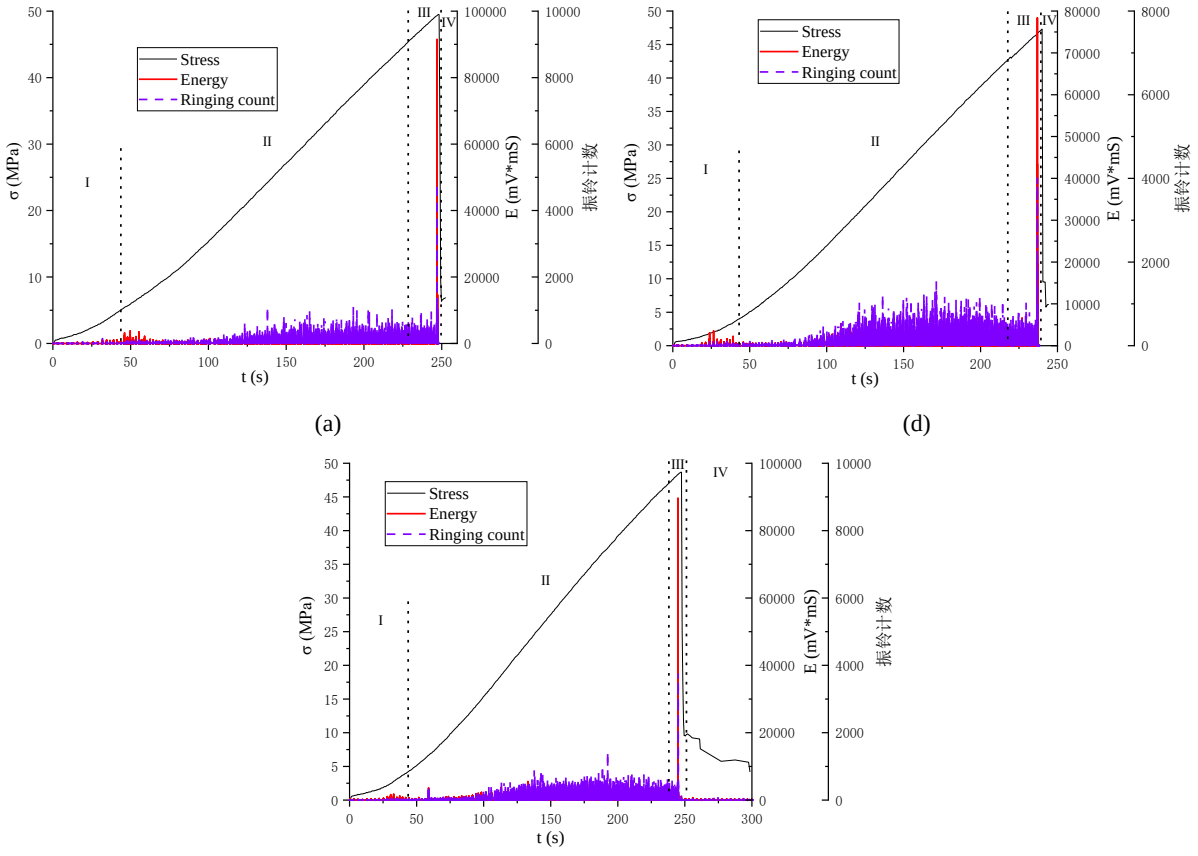


FIGURE 13: AE characteristics. (a)*f*=1Hz. (b)*f*=2Hz. (c)*f*=4Hz. (d)*f*=10Hz. (e)*f*=20Hz.

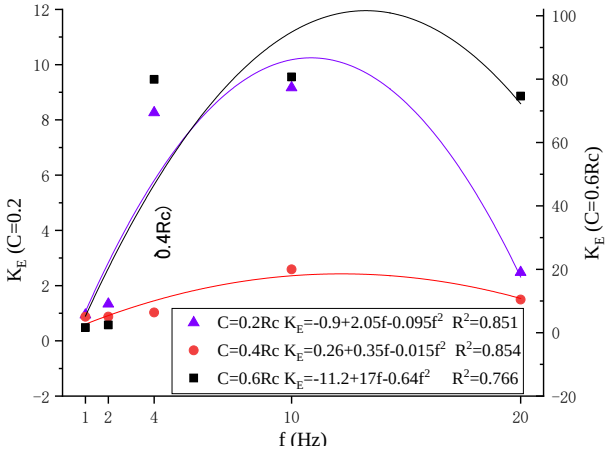
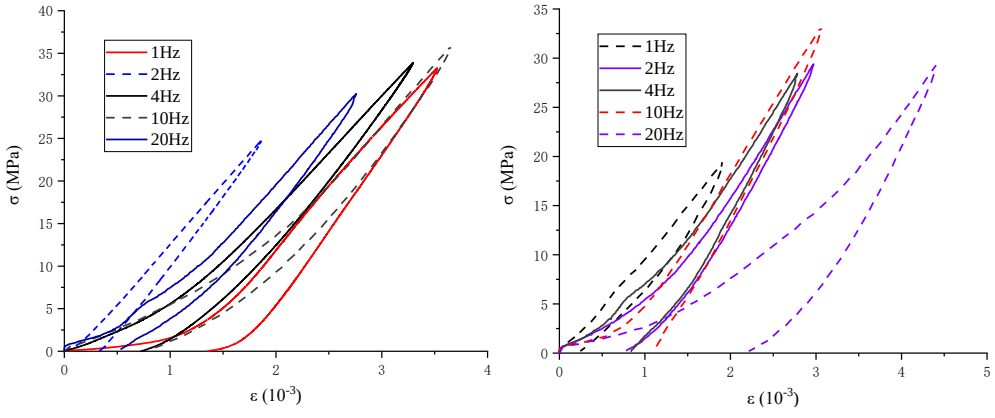
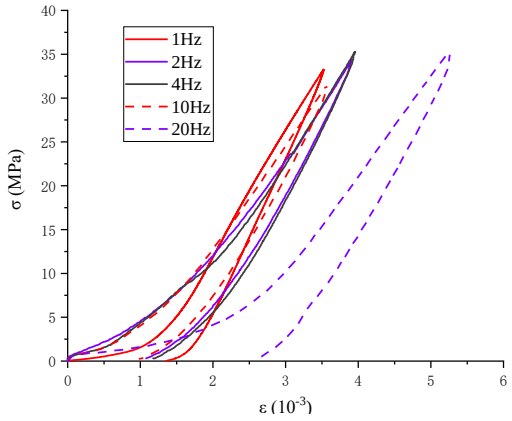


FIGURE 14: Impact energy index after fatigue





(c)

FIGURE 15: Loading and unloading curves of each sample group. (a)C=0.2σ_c. (b)C=0.4σ_c. (c)C=0.6σ_c.

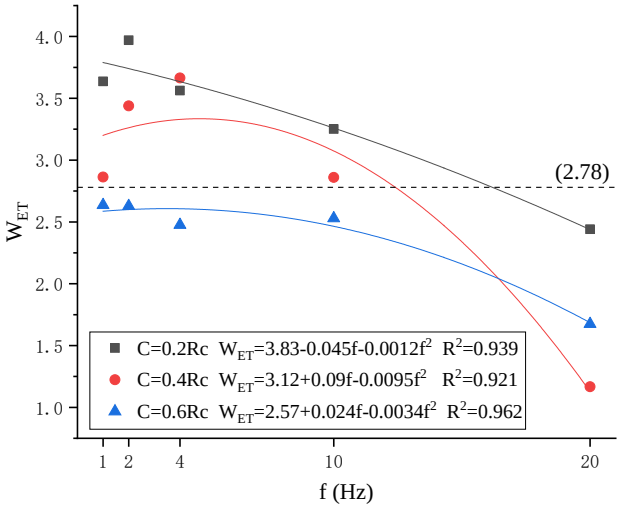


FIGURE 16: Elastic energy index after fatigue

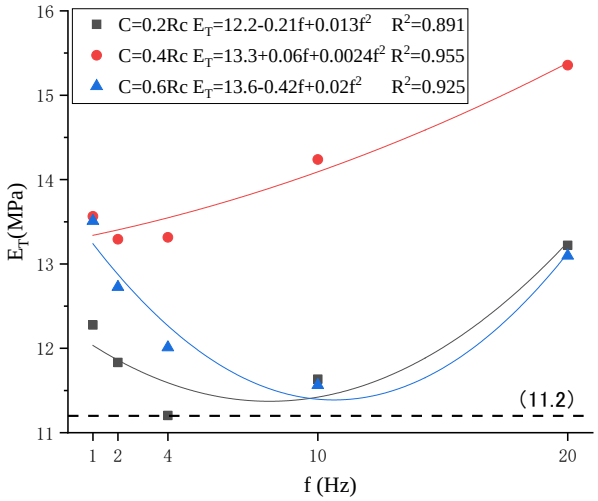


FIGURE 17: Elastic modulus

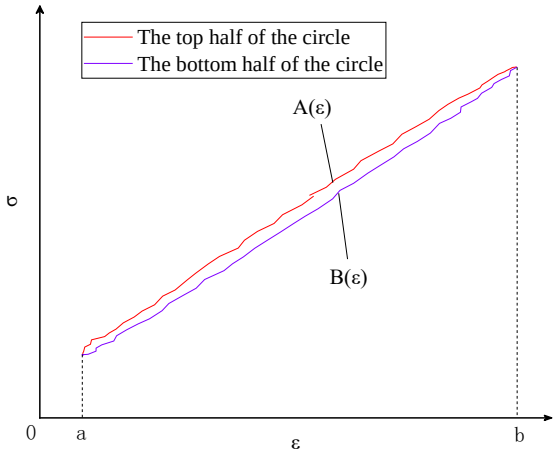


FIGURE 18: Schematic diagram of hysteresis loop area calculation

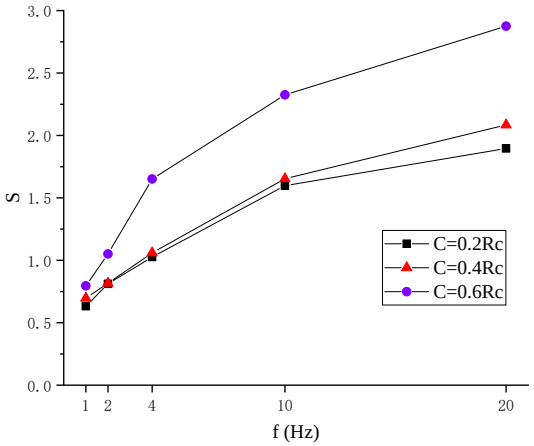


FIGURE 19: Hysteresis loop area point diagram

TABLE 1: Types of fatigue loading test

Group	*C*	*A*/MPa	*f*/Hz	*t*/s
I	$0.2\sigma_c$	4.5	1 2 4 10 20	500
II	$0.4\sigma_c$	4.5	1 2 4 10 20	500
III	$0.6\sigma_c$	4.5	1 2 4 10 20	500

TABLE 2: Wave speed data statistics

Group	v_0（m/s）	v_p（m/s）	SD_0	SD_p
I	3359.34	3414.67	65.54	39.33
II	3396.22	3400.45	49.06	71.19
III	3348.76	3412.78	87.27	91.74

TABLE 3: Fatigue loading damage variable

t/s	f=1Hz	f=2Hz	f=4Hz	f=10Hz	f=20Hz
1	0.142	0.133	0.137	0.117	0.106
50	0.176	0.159	0.163	0.140	0.144
150	0.192	0.176	0.169	0.150	0.154
250	0.200	0.184	0.171	0.160	0.165
350	0.207	0.187	0.173	0.165	0.170
450	0.211	0.193	0.174	0.173	0.176

TABLE 4: Strain statistics

t/s	Axial strain（10^{-3}）					Hoop strain （10^{-3}）					Volumetric strain （10^{-3}）				
	1Hz	2Hz	4Hz	10Hz	20Hz	1Hz	2Hz	4Hz	10Hz	20Hz	1Hz	2Hz	4Hz	10Hz	20Hz
50	3.34	3.35	2.95	3.47	2.47	-0.050	-0.114	-0.052	-0.088	-0.047	3.43	3.58	3.05	3.64	2.57
150	3.38	3.40	2.96	3.50	2.49	-0.049	-0.116	-0.048	-0.091	-0.048	3.44	3.63	3.06	3.68	2.59
250	3.41	3.42	2.97	3.53	2.56	-0.051	-0.116	-0.044	-0.090	-0.048	3.51	3.65	3.05	3.71	2.61
350	3.43	3.44	2.97	3.54	2.53	-0.052	-0.116	-0.044	-0.091	-0.048	3.52	3.67	3.06	3.72	2.62
450	3.44	3.45	2.97	3.57	2.54	-0.052	-0.116	-0.043	-0.093	-0.048	3.54	3.69	3.06	3.75	2.64

TABLE 5: Rock burst parameters tested before and after fatigue

C	f/Hz	σ_c/MPa	$\varepsilon/10^{-3}$	K_E	W_{ET}	E_T/GPa
Before fatigue		45.7	4.31	1.72	2.78	11.2
$0.2\sigma_c$	1	42.2	3.85	0.94	3.64	12.3
	2	34.4	3.30	1.34	3.97	11.8
	4	46.0	4.19	8.26	3.56	11.2
	10	50.8	4.43	9.17	3.25	11.6
	20	52.1	4.74	2.48	3.62	13.2
$0.4\sigma_c$	1	47.4	4.51	0.87	2.86	13.6
	2	41.5	4.39	0.88	3.44	13.3
	4	48.4	4.09	1.03	2.44	13.3
	10	47.2	4.37	2.59	2.86	14.2
	20	44.2	3.90	1.49	1.17	15.4
$0.6\sigma_c$	1	48.7	4.28	1.63	2.64	13.5
	2	43.1	4.99	2.45	2.63	12.7
	4	49.7	4.97	79.93	2.48	12.0
	10	45.6	4.74	80.69	2.53	11.6
	20	50.3	4.84	74.65	1.67	13.1